Proceedings World Geothermal Congress 2026
Calgary, Canada, June 8 – 11, 2026

Critical Fiber Length and Distribution Effects on Fracture Sealing in Geothermal Systems: A CFD–DEM Study

Zhengxun Hui, Arash Dahi Taleghani*

Department of Energy and Mineral Engineering, The Pennsylvania State University, State College, PA, 16801, USA*

arash.dahi@psu.edu

Keywords: geothermal drilling, lost circulation materials, fiber sealing, CFD–DEM simulation, fiber design.

ABSTRACT

Geothermal systems hold great potential for future clean energy and carbon reduction strategies. However, their development is often constrained by fluid loss, where working fluids leak into the formation, reducing overall energy recovery efficiency. In this study, a coupled CFD–DEM (Computational Fluid Dynamics-Discrete Element Method) framework was employed to simulate the evolution of fiber-based lost circulation materials (LCMs) with different length distributions (uniform, normal, and bimodal), and to evaluate their structural stability under geothermal conditions. The results indicate that an average fiber length of approximately 7.7 mm serves as a critical threshold, beyond which stable fiber networks can be formed. Moreover, increasing the standard deviation of the length distribution significantly enhances network robustness, improving pressure-bearing capacity by about 20% and enabling sustained selective regulation of fluid flow. Under low-viscosity fluid conditions, the bridging process requires more time and exhibits reduced stability. These findings provide valuable insights into geothermal development under high-temperature conditions. The work proposes an interdisciplinary fiber network design framework that can offer theoretical guidance for improving energy recovery efficiency and extending the lifespan of geothermal reservoirs.

1 INTRODUCTION

Geothermal energy is increasingly recognized as a promising solution for meeting the growing global demand for safe, sustainable, and carbon-neutral energy. However, geothermal drilling faces some of the most extreme downhole conditions encountered in subsurface operations, including elevated temperatures, high pressures, and heterogeneous fractured formations (Ji et al., 2025; Liu et al., 2025; Zhang et al., 2025). Among the many challenges, lost circulation, which is the uncontrolled loss of drilling fluids into surrounding formations, remains one of the most frequent and costly complications (Lavrov, 2016). Lost circulation not only causes excessive fluid consumption and reduced penetration rates but can also trigger stuck pipe incidents, remedial fishing operations, or, in severe cases, well control emergencies (Hui et al., 2024). For geothermal wells where the drilling margin is extremely narrow, the consequences are particularly severe, often resulting in prolonged non-productive time and significantly increased costs (Legarth et al., 2005; Hu et al., 2021; Li et al., 2016; Liu et al., 2020).

To mitigate lost circulation, lost circulation materials (LCMs) are commonly deployed as physical barriers to seal fractures and restore wellbore stability (Feng et al., 2018). Traditional granular LCMs, though widely used, often exhibit poor sealing efficiency and limited structural stability under irregular and evolving fracture geometries. In contrast, fiber-based LCMs have demonstrated superior performance due to their flexibility, entanglement potential, and ability to form multi-scale bridging networks. Field and laboratory studies indicate that fiber networks can create mechanically stable sealing structures, substantially reducing fluid loss even under complex flow conditions (Nayberg, 1987; Alsabagh et al., 2014; Amanullah et al., 2020). This makes fiber-based materials a promising candidate for geothermal drilling, where the sealing medium must withstand both high temperatures and dynamic fluid disturbances.

In recent years, numerical simulation has emerged as a powerful tool for unraveling the complex behaviors of LCMs within fractured media (Lee, 2022; Cassian, 2024). CFD–DEM models allow detailed tracking of fiber transport, deformation, and entanglement under flow conditions, providing unprecedented mechanistic insights (Cundall and Strack, 1979; Zhong et al., 2016; Zeng et al., 2016; G. Zhang et al., 2017; Zheng et al., 2020). These models have been used to identify critical parameters such as fiber length, stiffness, and concentration, and to predict the evolution of plugging structures over time. Yet, most existing studies remain restricted to isothermal or water-based fluid systems. The influence of high-temperature geothermal environments, where drilling fluids experience significant viscosity reduction and enhanced thermal convection, has received limited attention. Under such conditions, fibers may soften, and the combined effects of buoyancy, low viscosity, and

temperature gradients can destabilize otherwise robust seals. A systematic investigation of these mechanisms is therefore lacking, limiting the ability to design LCMs optimized for geothermal drilling operations.

The present study addresses this gap by integrating drilling-stage fiber-LCM design within a geothermal context using a unified CFD–DEM framework. First, we identify the critical mean fiber length and the role of length distribution in establishing stable seals within fractured geometries, revealing how bimodal length distributions can enhance entanglement and accelerate plugging. Second, we extend the analysis to geothermal-like conditions by employing a low-viscosity fluid to represent the effect of elevated temperature, capturing the destabilizing influence of thermal and flow disturbances on established fiber networks. These results provide new insights into the performance limits of fiber-based LCMs under geothermal conditions and establish a foundation for optimizing material design in geothermal drilling systems.

2 METHODOLOGY

This study establishes a three-dimensional numerical framework based on the coupled CFD-DEM to systematically investigate the transport, deformation, and entanglement behavior of fiber-based LCMs within wedge-shaped fracture geometries under multi-phase flow conditions. In the model, fibers are represented using elastic beam theory, enabling the realistic simulation of complex deformation behaviors such as bending, buckling, and twisting under hydrodynamic forces, while accurately reproducing their micro-scale trajectories and contact aggregation processes. Within this framework, we systematically vary the injection concentration, fiber length, and length distribution to evaluate their effects on the initiation time of plugging, pressure drop evolution, and network stability. These metrics reveal the intrinsic connection between fiber network self-organization and macroscopic sealing performance, providing a novel pathway for the structural optimization and engineering design of fiber-based LCMs.

2.1 Governing equations

The modeling framework integrates an Eulerian-based CFD module for the continuous fluid phase with a Lagrangian-based DEM module for the discrete particulate phase. Information between the two modules is exchanged in a two-way coupled manner, allowing both the fluid and solid phases to influence one another. This coupling is essential for simulating the evolution of particle-laden flows and the dynamic plugging process. The fluid flow is governed by the volume-averaged Navier–Stokes equations, including：

$$\frac{\partial(\rho_f \varepsilon_f u)}{\partial t} + \nabla \cdot \left(\rho_f \varepsilon_f u\right) = 0 \tag{1}$$

Navier-Stokes equation for the momentum conservation (Malvern, 1969) is:

$$\frac{\partial(\rho_f \varepsilon_f u)}{\partial t} + \nabla \cdot \left(\rho_f \varepsilon_f uu\right) = \frac{-1}{\rho}\nabla p - \nabla \cdot \tau_f + \rho_f \varepsilon_f g - F \tag{2}$$

where ρ_f denotes the fluid density, ε_f is the fluid volume fraction, u is the average fluid velocity, ∇p is the pressure gradient across the fluid cell, τ_f the viscous stress tensor, g the gravitational acceleration, and F the interaction force exerted by the suspended particles on the fluid.

The solid phase is modeled using the DEM, which resolves the translational and rotational motions of each particle according to Newton's second law (Cundall and Strack, 1979):

$$m_p \frac{dv_p}{dt} = F_s + F_b \tag{3}$$

$$I_p \frac{d\omega_p}{dt} = M_b + \sum (rc \times F_{cm} + M_{cm}) \tag{4}$$

where Fd is the drag force, Fp is the pressure gradient force, Fg is the force applied due to gravity, and Fc is the summation of all the contact forces accumulated from inter-particle and particle-boundary interactions from the fluid phase. Drag coefficients are computed using the Di Felice model (Di Felice, 1994), and contact forces are solved using Hertz-Mindlin contact model:

$$Fd = 12 C_d \rho A_p |V_s| V_s \tag{5}$$

$$C_d = \left(0.63 + \frac{4.8}{\sqrt{\varepsilon_i Re_p}}\right)^2 \varepsilon^{2-\zeta} \tag{6}$$

$$\zeta = 3.7 - 0.65 e^{\left[-0.5(1.5-\log[\varepsilon Rep])^2\right]} \tag{7}$$

where Cd is the drag coefficient of the particle, ρ is the density of the fluid, Vs is the particle slip velocity, Ap is the cross-sectional area of the particle, ε_i is the void fraction of the grid cell pertaining to the particle and R_{ep} is the particle Reynolds number. Linear spring contact model for fibrous elements is:

$$F_c = F_n n + F_t t \tag{8}$$

where F_n and F_t are the normal and tangential components of the respective contact forces. n and t are the normal and tangential contact vectors, respectively.

$$F_n = -K_n d_n - N_n \vartheta_n \tag{9}$$

$$F_t = -K_t dt - N_t \vartheta_t \; if \; |K_t dt| < |K_n d_n| C_{fs} \tag{20}$$

$$else \; F_t = \frac{|K_n dn| C_{fs} dt}{|dt|} \tag{31}$$

Fibers are modeled as chains of cylindrical sub-elements connected by virtual springs to simulate axial and bending stiffness. This structure enables realistic deformation, folding, and entanglement in response to fluid forces. The bending stiffness is computed using Euler–Bernoulli beam theory:

$$k_n = \frac{EA}{L}, \; k_b = \frac{EI}{L} \tag{42}$$

where E is Young's modulus, A is the cross-sectional area, I is the moment of inertia, and L is the segment length. This structure enables the simulation of both soft and stiff fibers and their distinct bridging modes (entanglement vs. nesting), a key advancement from previous models, which lacked the ability to represent fiber flexibility. For a given time step of the fluid phase solver, the DEM time step is determined based on the Rayleigh wave propagation time across a particle (Rayleigh, 1885):

$$\tau = \frac{\pi R}{V_{Rayleigh}} \tag{53}$$

where R is the radius of the sphere and $V_{Rayleigh}$ is the Rayleigh wave velocity within the particle.

The dimensionless time is used to evaluate the efficiency of the sealing in different-sized fractures:

$$t_d = \frac{V_{cum.inj.}}{V_{frac}} \tag{64}$$

where V_{frac} is the volume of the fracture and $V_{cum.inj.}$ is the cumulative volume of fluid injected. This enables an evaluation of the plugging time devoid of the influence of the fracture geometry

2.2 Model Description and Setup

We employed STAR-CCM+ 18.02.008-R8 (Siemens Digital Industries Software, 2023) for coupled simulations, combining the Navier–Stokes equations to model fluid flow (CFD component) with the DEM to capture the motion, deformation, and contact behavior of fibers. The fibers were modeled using elastic beam theory, enabling the simulation of bending, buckling, and twisting during transport. This approach allows the model to capture both the entanglement characteristics of flexible fibers and the bridging behavior of stiffer fibers. The DEM time step was set to 10^{-7}s, while the CFD time step was set to 10^{-5}s. To ensure numerical stability, the mesh was refined such that the fiber diameter was smaller than the minimum cell length, and mesh smoothing was applied to enhance the recognition of slender fibers. Figure 1 shows the constructed wedge-shaped fracture flow model, which was used to simulate the plugging process of fiber-based LCMs. The fracture geometry includes a length of 80 mm, a height of 10 mm, an inlet width of 6 mm, and an outlet width of 2 mm.

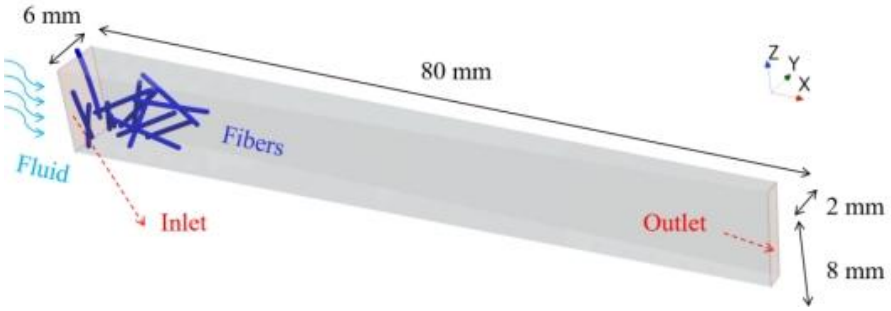


Figure 1. Schematic of the wedge-shaped fracture geometry

The fluid was defined as an incompressible Newtonian fluid with a viscosity of 0.08 Pa·s and a density of 1700 kg/m^3. A pressure difference of 95,000 Pa (95 kPa) was applied between the fracture inlet and outlet, with gravity acting along the Z-axis. The fiber diameter was set to 550 μm, with a Young's modulus of 1 GPa, Poisson's ratio of 0.2, and particle–particle static friction coefficient of 0.5, while the particle–wall friction coefficient was 0.71. For the fiber component, the Young's modulus was assigned as 0.01 GPa, Poisson's ratio as 0.2, and coefficient of restitution as 0.5. The static friction coefficients were set to 0.9 for fiber-fiber, 0.71 for fiber-wall, and 0.5 for fiber-particle interactions. A no-slip boundary condition was applied to the fracture walls to realistically simulate the interaction between the viscous fluid and the solid surfaces. During the simulation, flow velocity and outlet mass flow rate were monitored to determine the occurrence of plugging, and after sealing was achieved, the Maximum Plugging Pressure (MPP) was measured to assess the mechanical stability of the formed structure.

To systematically investigate the influence of key parameters, three core variables were examined: fiber length distribution, fiber stiffness, and injection concentration. After preliminary screening of multiple concentrations, a 15% volume fraction (corresponding to a mass flow rate of 0.06 kg/s) was selected as the standard injection concentration. The fiber length distributions included three typical types: uniform, normal, and bimodal. For the uniform distribution, seven representative samples with different average lengths and zero standard deviation were used. These samples had aspect ratios ranging from 30 to 160, corresponding to fiber lengths from 1.65 mm to 8.8 mm.

To validate the accuracy of the model, the simulated pressure drop results under three fiber length distributions were compared with the experimental data from de Godoi et al. (2018) for wedge-shaped fractures. Under a flow velocity of 1.5 m/s, the simulated pressure drop was approximately 5500 Pa, which closely matches the experimental value, indicating that the constructed CFD–DEM model effectively captures the micro-mechanical behavior of the fiber–fluid system. Moreover, the pressure drop curves under various parameter conditions exhibited good numerical stability, further confirming the convergence and reliability of the model. The model was also evaluated under fiber-free conditions by varying the flow rate to examine the pressure–flow response. As shown in Fig. 2, the CFD predictions show excellent agreement with the expected viscous–inertial pressure–flow relationship, consistent with classical resistance correlations (Ergun, 1952). The pressure drop increases nonlinearly with mass flow rate, confirming that the model captures the dominant flow resistance mechanisms. In addition, simulations with different random fiber injection realizations produced similar plugging behavior, indicating the robustness of the predicted sealing mechanism.

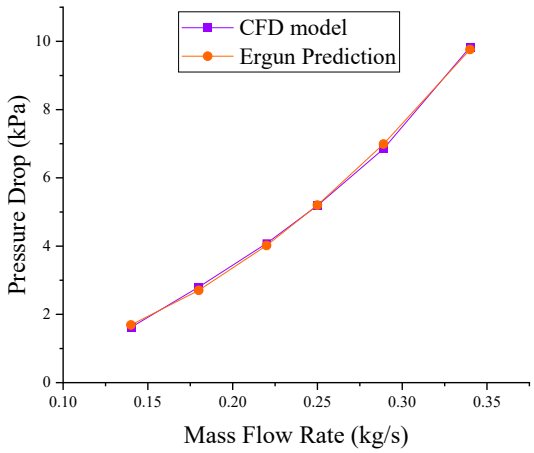


Figure 2. Validation of the pressure drop between the CFD model and the Ergun prediction under fiber-free conditions.

3 RESULTS AND DISCUSSION

3.1 Evolution of sealing structure during the bridging process

Figure 3 illustrates the progressive evolution of fiber motion within the fracture. At the early stage, fibers are dispersed and transported downstream with minimal interaction. As time progresses, fibers begin to accumulate at constriction zones, forming local clusters. With continuous fiber injection, these clusters interconnect into a coherent network, eventually developing into a mechanically stable sealing structure that resists further flow.

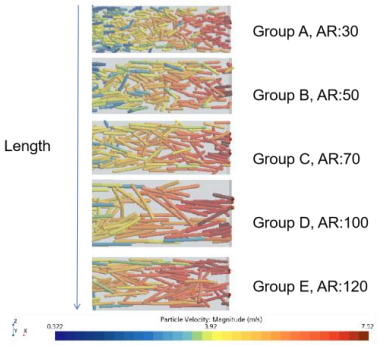


Figure 3. Evolution of fiber motion in different lengths during the plugging process

Figure 4 presents a time-sequence comparison of particle velocity distributions during the sealing process. Initially, fibers exhibit high transport velocities with limited interaction. Over time, localized bridging occurs, leading to progressive reduction in flow velocity. In the final stage, the majority of fibers are immobilized within the fracture, resulting in a stable seal and near-zero outlet velocity.

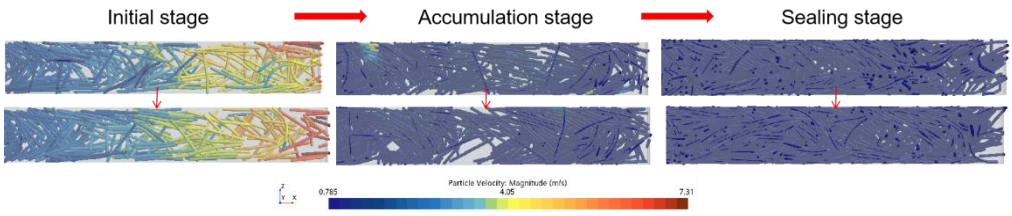


Figure 4. Evolution of three stages during the bridging process

3.2 Sealing Efficiency under Different Fiber Length Distributions

Figure 5 shows that, for normal and uniform distribution fiber lengths, similar trends in entanglement and plugging efficiency are observed. At lower aspect ratios, fibers fail to establish sufficient bridging and entanglement, resulting in unsuccessful sealing. When the aspect ratio reaches 140, the system undergoes a

critical transition, shifting abruptly from continuous leakage to effective plugging. All subsequent cases with higher aspect ratios achieve stable sealing, indicating that exceeding this threshold is a necessary condition for the formation of a robust, load-bearing fiber network. However, further increases in aspect ratio provide only marginal benefits while incurring higher material costs. This finding suggests that instead of relying solely on length extension, designing more complex structural combinations may be a more efficient strategy for achieving reliable sealing performance. For the bimodal distribution system, an equivalent aspect ratio was adopted as the evaluation metric. Figure 5(c) shows that effective sealing first occurs at an aspect ratio of 140. Beyond this threshold, all cases achieve successful plugging; however, the relationship is not linear. This finding suggests that sealing efficiency is not governed solely by fiber length but is strongly influenced by the complexity of the length distribution. The synergy between long and short fibers plays a critical role in determining the formation of stable sealing structures.

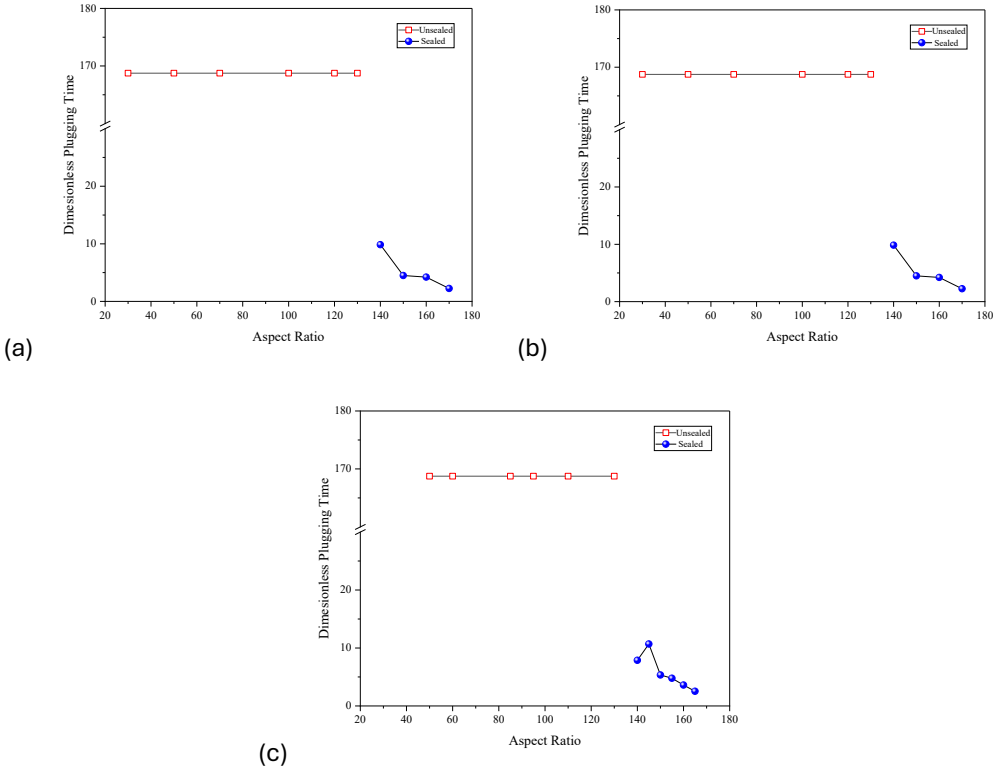


Figure 5. Dimensionless plugging time of (a) normal distribution, (b) uniform distribution and (c) bimodal distribution fibers in different aspect ratios.

3.3 Maximum Plugging Pressure under Different Fiber Length Distributions

Figure 6 illustrates the evolution of pressure drop during the sealing process for fiber length distributions of (a) normal, (b) uniform, and (c) bimodal. For all three cases, the unsealed scenarios (red squares) show negligible pressure drop, reflecting continuous fluid leakage without effective bridging. In contrast, the sealed cases (blue circles) exhibit a sharp increase in pressure drop once a stable fiber network is formed, followed by sustained load-bearing capacity. While the critical transition occurs at a similar aspect ratio (~140) across all distributions, the bimodal system demonstrates more efficient entanglement, leading to faster stabilization and slightly higher sealing robustness compared to uniform or normal distributions. These results confirm that not only the mean fiber length but also the distribution complexity plays a decisive role in fracture sealing performance.

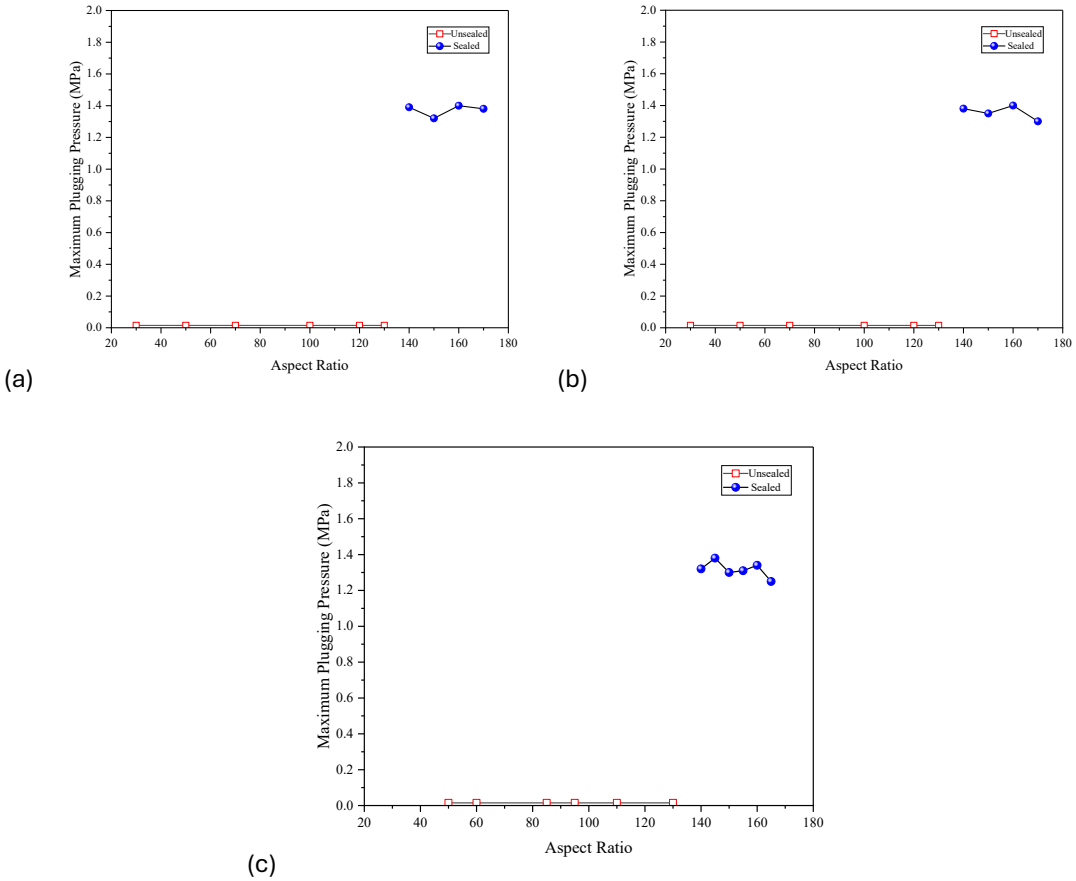


Figure 6. Maximum plugging pressure of (a) normal distribution, (b) uniform distribution, and (c) bimodal distribution.

3.4 Stability of the sealing structure using low viscosity fluid

Figure 7 compares the evolution of fiber motion under base-viscosity and reduced-viscosity fluid conditions. Both cases correspond to configurations that achieved successful sealing in the previous simulations; the fluid viscosity was modified to isolate its effect. In both cases, fibers initially accumulate near the fracture inlet, where local convergence of streamlines promotes the formation of potential bridging zones. However, when the fluid viscosity is reduced, the hydrodynamic forces acting on the fibers become dominant over the cohesive and frictional resistance of the forming network. Consequently, the incipient bridging clusters visible near the inlet are gradually dispersed, and the fibers are swept downstream toward the fracture outlet, where the flow velocity is highest. This continuous erosion of the bridging structure prevents the establishment of a stable plug. The results clearly demonstrate that viscosity reduction undermines the integrity of fiber entanglement and substantially delays or even inhibits complete sealing. This finding is particularly relevant to geothermal drilling systems using high-temperature or CO_2-based fluids, where the intrinsic viscosity of the working fluid is considerably lower than that of conventional water-based muds.

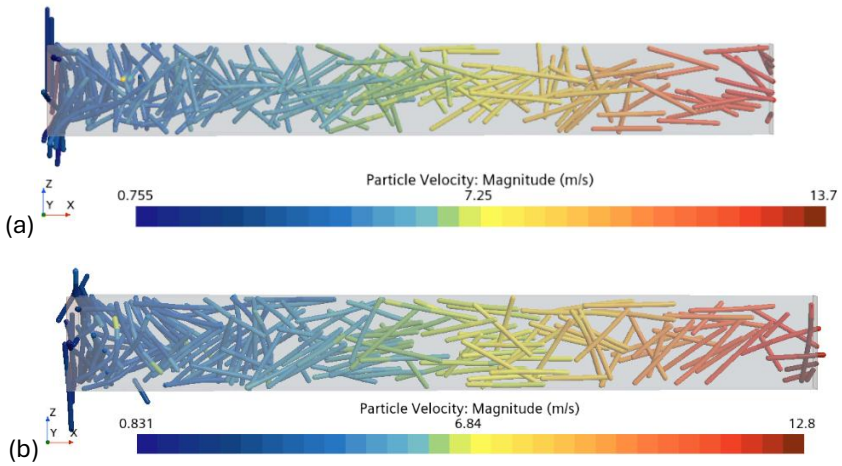


Figure 7. Particle velocity of fibers under low-viscosity conditions, showing unstable bridging and failure to form sealing structures (a, bimodal distribution case; b, normal distribution case)

4 CONCLUSION

This study employed a coupled CFD–DEM framework to systematically investigate the bridging and sealing behavior of fiber-based lost circulation materials (LCMs) in geothermal fracture systems. The results reveal that an average fiber length of approximately 7.7 mm serves as a critical threshold for successful bridging: fibers shorter than this value fail to form stable networks, while those beyond it consistently achieve effective sealing. Moreover, the distribution of fiber lengths plays a decisive role—broader or bimodal distributions substantially enhance network robustness, as the synergy between long and short fibers accelerates entanglement, reduces plugging time, and improves the pressure-bearing capacity by nearly 20%. The sealing process is found to evolve progressively from dispersed clusters to coherent load-bearing networks, with a rapid transition to stability once the aspect ratio exceeds the critical range. Under low-viscosity conditions, such as high-temperature or CO_2-based drilling fluids, initial bridges are easily disrupted by hydrodynamic drag, leading to unstable sealing behavior. These findings collectively provide a mechanistic understanding of fiber network evolution and highlight the necessity of tailoring LCM design to account for viscosity reduction and geothermal disturbances. Overall, this work establishes quantitative design principles for optimizing fiber geometry and distribution, offering practical guidance for enhancing wellbore stability, improving lost circulation control in geothermal systems.

Acknowledgements

The authors declare that no specific funding or external support was received for this work.

REFERENCES

Alaskar, M., Ames, M., Connor, S., Liu, C., Cui, Y., Li, K., & Horne, R. Nanoparticle and microparticle flow in porous and fractured media—An experimental study. SPE Journal, 17(04), (2012), 1160–1171. https://doi.org/10.2118/146752-PA

Amanullah, M., Alouhali, R., & AlArfaj, M. A Date Tree Fiber-Based LCM for Severe Loss Control. International Petroleum Technology Conference, Dhahran, Saudi Arabia, (2020). https://doi.org/10.2523/IPTC-20165-MS

Cassian, H., & Dahi Taleghani, A. Fiber Stiffness: An Essential Parameter of the Effectiveness of Fiber-Based Lost Circulation Materials—A CFD-DEM Numerical Investigation. SPE Journal, 29, (2024), 1303–1320. https://doi.org/10.2118/218377-PA

Cundall, P. A., & Strack, O. D. L. A Discrete Numerical Model for Granular Assemblies. Geotechnique, 29(1), (1979), 47–65. https://doi.org/10.1680/geot.1979.29.1.47

Di Felice, R. The Voidage Function for Fluid-Particle Interaction Systems. International Journal of Multiphase Flow, 20(1), (1994), 153–159. https://doi.org/10.1016/0301-9322(94)90011-6

Ergun, S. 1952. Fluid Flow Though Packed Columns. Chem Eng Prog 48: 89–94.

Felipe Augusto Paes de Godoi, et al. Study of the pressure drop and the flow of loss circulation material suspensions in a physical simulator of fractures, Journal of Petroleum Science and Engineering, 168, 2018, 48-58, https://doi.org/10.1016/j.petrol.2018.04.031.

Feng, Y., & Gray, K. E. Modeling Lost Circulation Through Drilling-Induced Fractures. SPE Journal, 23(1), (2018), 205–223. https://doi.org/10.2118/187945-PA

Henriques Cassian, & Dahi Taleghani, A. Fiber Stiffness: An Essential Parameter of the Effectiveness of Fiber-Based Lost Circulation Materials—A CFD-DEM Numerical Investigation. SPE Journal, 29, (2024), 1303–1320. https://doi.org/10.2118/218377-PA

Hu, X., Song, X., Wu, K., Shi, Y., & Li, G. Effect of proppant treatment on heat extraction performance in enhanced geothermal system. Journal of Petroleum Science and Engineering, 207, (2021), 109094. https://doi.org/10.1016/j.petrol.2021.109094

Hui, Z., Liu, W., Jia, G., Sun, H., & Tian, C. Numerical Analysis on Casing Deformation During Hydraulic Fracturing of Deep and Tight Volcanic Reservoir. Computational and Experimental Simulations in Engineering, ICCES 2023. Shenzhen, China (2024). https://doi.org/10.1007/978-3-031-42515-8_70

Ji, K., Zhang, Q., & Dahi Taleghani, A. Thermal short-circuit mitigation in enhanced geothermal systems: A novel dynamic flow regulation technology using temperature-sensitive viscosity modifiers. Energy Conversion and Management, 343, (2025), 120196. https://doi.org/10.1016/j.enconman.2025.120196

Lavrov, A. Lost Circulation: Mechanisms and Solutions. Cambridge, MA: Gulf Professional Publishing/Elsevier (2016).

Lee, L., & Dahi Taleghani, A. Assessment of Lost Circulation Material Particle-Size Distribution on Fracture Sealing: A Numerical Study. SPE Drilling & Completion, 37(3), (2022), 191–205. https://doi.org/10.2118/209201-PA

Legarth, B., Huenges, E., & Zimmermann, G. Hydraulic fracturing in a sedimentary geothermal reservoir: Results and implications. International Journal of Rock Mechanics and Mining Sciences, 42(7–8), (2005), 1028–1041. https://doi.org/10.1016/j.ijrmms.2005.05.014

Li, T., Shiozawa, S., & McClure, M. W. Thermal breakthrough calculations to optimize design of a multiple-stage enhanced geothermal system. Geothermics, 64, (2016), 455–465. https://doi.org/10.1016/j.geothermics.2016.06.015

Liu, H., Wang, H., Lei, H., Zhang, L., Bai, M., & Zhou, L. Numerical modeling of thermal breakthrough induced by geothermal production in fractured granite. Journal of Rock Mechanics and Geotechnical Engineering, 12(4), (2020), 900–916. https://doi.org/10.1016/j.jrmge.2020.01.002

Liu, S., & Dahi Taleghani, A. Engineering of polymer nanocomposites using acid-functionalized graphite nanoplatelets for high-temperature sealing purposes. Composites Part B: Engineering, (2025), 112772.

Malvern, L. E.Introduction to the Mechanics of a Continuous Medium. Englewood Cliffs, New Jersey, USA (1969).

Nayberg, T. M. Laboratory Study of Lost Circulation Materials for Use in Both Oil-Based and Water-Based Drilling Muds. SPE Drilling Engineering, 2(3), (1987), 229–236. https://doi.org/10.2118/14723-PA

Rayleigh, L. On Waves Propagated along the Plane Surface of an Elastic Solid. Proceedings of the London Mathematical Society, s1-17(1), (1885), 4–11. https://doi.org/10.1112/plms/s1-17.1.4

Siemens Digital Industries Software. STAR-CCM+, Version 18.02.008-R8, 2023.

Zeng, J., Li, H., & Zhang, D. Numerical simulation of proppant transport in hydraulic fracture with the upscaling CFD-DEM method. Journal of Natural Gas Science and Engineering, 33, (2016), 264–277. https://doi.org/10.1016/j.jngse.2016.05.030

Zhang, G., Gutierrez, M., & Li, M. A coupled CFD-DEM approach to model particle-fluid mixture transport between two parallel plates to improve understanding of proppant micromechanics in hydraulic fractures. Powder Technology, 308, (2017), 235–248. https://doi.org/10.1016/j.powtec.2016.11.055

Zhang, Q., & Dahi Taleghani, A. Downhole flow control: A key for developing enhanced geothermal systems in horizontal wells. Renewable Energy, 237, (2024), 121578.

Zheng, Y., Wang, H., Yang, B., Hu, Y., Shen, Z., Wen, H., & Yan, W. CFD-DEM simulation of proppant transport by supercritical CO_2 in a vertical planar fracture. Journal of Natural Gas Science and Engineering, 84, (2020), 103647. https://doi.org/10.1016/j.jngse.2020.103647

Zhong, W., Yu, A., Liu, X., Tong, Z., & Zhang, H. DEM/CFD-DEM modeling of non-spherical particulate systems: Theoretical developments and applications. Powder Technology, 302, (2016). 108–152.